mater.scichina.com link.springer.com

Published online 30 May 2023 | https://doi.org/10.1007/s40843-023-2453-x
Sci China Mater 2023, 66(8): 3292–3299

An ecofriendly and efficient wood-based polyoxovanadate solar evaporation generator

Tian Zhang, Wen Yan, Yan Wang, Jie Wang, Congyan Liu, Fei Ye and Bo Liu*

ABSTRACT **Currently, freshwater scarcity is a global challenge, and developing low-cost methods for purifying, desalinating, and distilling seawater is crucial. Natural wood, owing to its advantages of high hydrophilicity, low density, microporous channels, and low thermal conductivity, is widely considered a vehicle for solar evaporation. However, the majority of the reported wood-based solar evaporation generators have been economically inefficient, with limited evaporation rates under low-power solar irradiation. Herein, we developed an ecofriendly and efficient wood-based solar evaporation generator comprising a material with excellent photothermal conversion efficiency, polyoxovanadate, loaded on the wood surface with a natural channel structure. The solar evaporation generator exhibited high light absorption capacity (~98%) in the wide wavelength range of 200–1200 nm, rapid water transport through the wood channels, minimal heat dissipation due to the adiabaticity of the wood, and reduced evaporation enthalpy. Therefore, the overall evaporation efficiency was increased, and a high evaporation rate of 2.23 kg m^{-2} h^{-1} and solar-vapor efficiency of 90% under 1 Sun was observed. This environment-friendly, low-cost, and high-efficiency evaporation generator has enormous potential for practical applications in solar desalination and water purification.**

Keywords: solar evaporation, polyoxovanadate, desalination, wood, ecofriendly

INTRODUCTION

The shortage of freshwater has become one of the most crucial global challenges in society [1,2]. To address this issue, various separation techniques, such as membrane or distillation processes and reverse osmosis technologies, have been implemented to purify water at an industrial scale [3–5]. Nevertheless, these technologies require complicated procedures and thus suffer from high cost and low economic efficiency [6,7]. Solar evaporation and desalination with green and free solar energy as the main energy source are emerging technologies with ecofriendly and efficient advantages [8–10]. Efficient solar-to-thermal energy conversion as a prerequisite for solar evaporation has been achieved using various photothermal materials, such as locally heated metal plasma particles [11,12], carbon materials with broadband spectral absorption and hydrophilic surfaces [13,14], and black-appearing organic polymers [15–17], which convert solar energy for green, efficient, and long-term water evaporation.

In addition to efficient solar-to-thermal energy conversion, ensuring water transport management of the photothermal material surface is important to achieve efficient and continuous solar evaporation. Photothermal conversion and water transport are usually achieved using separate components owing to their distinct functions and material characteristics. Typical materials selected for water transport feature hierarchical porosity, hydrophilicity, and heat insulation [18–20]. Inspired by water transport in plants, researchers have utilized wood as water transport media, and it is particularly suitable for industrial-scale applications, with unique advantages of hydrophilicity, low density, naturally existing water transport microchannels, excellent thermal insulation properties, and low cost [15,21], compared with common carriers such as insulating and absorbent foams [18], mesoporous glass [19], glass beads [20], and hydrogels [22,23]. Moreover, the larger-vessel channels and narrower tracheid channels in natural wood prevent surface salt precipitation phenomena during the accelerated evaporation process because a planar salt concentration gradient is naturally and spontaneously formed during seawater evaporation [24,25]. Such unique hydrophilic channel structures also reduce the change in water evaporation enthalpy, owing to the affinity between the channel wall and water [26]. Smart designs involving wood carbonization on surfaces, which enables photothermal conversion, have been implemented to integrate photothermal conversion and water transport for solar evaporation [24]; however, the carbonized layer exhibits low photothermal conversion efficiency and thus results in a relatively low evaporation rate. Hydrogel-based solar evaporation has been adopted owing to its structural tunability and high performance [27,28]; however, it suffers from cumbersome preparation, which limits its practical applications.

Polyoxovanadate clusters with tunable structures and diverse functions have been applied in photocatalysis [29], thermoelectricity [30], radiokinetic therapy [31], sodium-ion batteries [32], and solar evaporation [19]. In this study, we applied polyoxovanadate clusters $[Ni(Phen)_3]_3[V_{15}O_{36}(Cl)]$ (hereinafter referred to as NiV_{15}) as light absorbers and loaded them to the surface of hydrophilic basswood to achieve continuous and efficient evaporation, owing to the timely water transport to the wood surface and the excellent photothermal conversion of NiV_{15}. Furthermore, the combination of insulating household melamine formaldehyde (MF) and a double-layer vacuum beaker concentrates the heat on the evaporation surface and reduces the energy loss caused by heat conduction to bulk water and the

School of Chemistry and Materials Science, University of Science and Technology of China, Hefei 230026, China
* Corresponding author (email: liuchem@ustc.edu.cn)

surrounding environment. Integrating the above advantages, the fabricated NiV_{15}@wood-based solar evaporation system could achieve rapid water evaporation (2.23 kg m^{-2} h^{-1}) under 1 Sun and 90% efficient evaporation efficiency, which are among the highest values reported for wood-based solar evaporation systems.

EXPERIMENTAL SECTION

Synthesis of polyoxovanadate clusters

Dark green crystals of $(Me_4N)_6[V_{15}O_{36}(Cl)]$ (hereinafter referred to as NV_{15}) were synthesized according to the procedure reported in the literature [33]. First, 0.95 g of mannitol (5.3 mmol, Shanghai Titan Scientific Co., Ltd.), 0.50 g of $(Me_4N)Cl$ (4.6 mmol, Sinopharm Chemical Reagent Co., Ltd.), and 1.08 g of NH_4VO_3 (9.2 mmol, Sinopharm Chemical Reagent Co., Ltd.) were added to a round-bottom flask containing 70 mL of pure water and magnetically stirred to make the reaction solution well mixed. Then, the mixture was boiled under reflux conditions for three days. At the end of the reaction, a dark blue-green solution was obtained, which was cooled to room temperature and left for a few days to precipitate dark green NV_{15} crystals.

Synthesis of $Ni(phen)_3Cl_2{\cdot}2H_2O$

$[Ni(phen)_3]Cl_2{\cdot}2H_2O$ was synthesized *via* a previously reported method [34]. $NiCl_2{\cdot}6H_2O$ (98%, Energy Chemical) and 1,10-phenanthroline monohydrate (98%, Aladdin) were added to a round-bottom flask according to the stoichiometric ratio of 1:3, and then, an appropriate amount of ethanol was added to dissolve all of the reagents to obtain a pink solution. The mixture was refluxed for ~45 min, and a precipitated pink product was obtained through the spin evaporation of the reaction solution. After being cooled to room temperature, the sample was added with excess anhydrous ethanol and then filtered and washed. The crude product was dissolved in a small amount of 50% hot ethanol, slowly cooled to 0°C, and recrystallized, then dried in an oven at 80°C to obtain the pink product $[Ni(phen)_3]Cl_2{\cdot}2H_2O$.

Fabrication of the evaporator

Basswood was purchased from the Alibaba Group, and the natural wood pieces were cut with a chainsaw into 1.5 cm × 1.5 cm × 0.2 cm rectangular pieces with a rough hair-like surface. The wood pieces were soaked in 20 mg mL^{-1} NV_{15} aqueous solution for 3 h. Afterward, the pieces were oven-dried at 80°C, and wood pieces with adsorbed NV_{15} crystals (NV_{15}@wood) were obtained. Subsequently, NV_{15}@wood was immersed into an aqueous $Ni(phen)_3Cl_2$ solution with three times the amount of adsorbed NV_{15} and allowed to react at 80°C for 12 h, so that the adsorbed NV_{15} on the surface was fully converted into NiV_{15} (Fig. S1). After the NV_{15}@wood with adsorbed NV_{15} was washed with water to remove the unreacted NV_{15}, NiV_{15}@wood was obtained and used as a heat collector chip for the evaporator. The amount of adsorbed NiV_{15} substances could be calculated from the mass of the wood pieces before and after adsorption.

Characterizations

The surface morphologies of natural wood and NiV_{15}@wood were determined using a Zeiss Gemini SEM500. The surface element distribution of NiV_{15}@wood composites was analyzed *via* a scanning electron microscope (SEM) coupled with an energy-dispersive spectrometer. The solar absorption properties of wood and NiV_{15}@wood under the wavelengths of 200–1200 nm were recorded by a SolidSpec-3700 ultraviolet-visible-near infrared (UV-vis-NIR) spectrometer. The concentrations of Na^+, Mg^{2+}, K^+, and Ca^{2+} in the collected desalinated water were determined *via* inductively coupled plasma mass spectrometry (Thermo Scientific iCAP 7000 SERIES). Contact angle testing was performed with an optical contact angle and interfacial tension meter (Kino SL200KS). Powder X-ray diffraction (PXRD) measurement was performed on a Rigaku MiniFlex 600 X-ray diffractometer using Cu Kα radiation (λ = 1.54178 Å).

Evaluation of evaporation performance

Evaporation rate calculation

The evaporation rate (v), which is an important indicator of the performance of the solar evaporation generator, was calculated according to Equation (1) [35]:

$$v = \frac{\mathrm{d}m}{S\mathrm{d}t}, \tag{1}$$

where m represents the evaporated mass of water, S is the practical area of the evaporation generator receiving illumination (a circle with a radius of 1.4 cm), and t is the duration of exposure to light. The evaporation rates of water (v_{water}) and the MF evaporation generator (v_{MF}) were obtained using the above Equation (1).

The water evaporation contributions of the MF around the evaporation chips of wood-MF and NiV_{15}@wood-MF need to be deduced; therefore, the following calculation was performed:

$$v_{NiV_{15}@wood} = \frac{\mathrm{d}m - v_{MF}S_{MF}\mathrm{d}t}{S_{NiV_{15}@wood}\mathrm{d}t}, \tag{2}$$

where $v_{NiV_{15}@wood}$ represents the evaporation rate of the NiV_{15}@wood evaporation generator, $S_{NiV_{15}@wood}$ represents the area of the NiV_{15}@wood evaporation chip (a square with a side length of 1.5 cm), and S_{MF} denotes the area of the MF (a circle with a radius of 1.4 cm minus the area of 1.5 cm^2).

Thermal efficiency calculation

The thermal conversion efficiency (η), which measures the ability of the input light energy to produce water steam, was calculated using Equation (3) [36]:

$$\eta = \frac{\dot{m}h_{LV}}{C_{opt}q_i}, \tag{3}$$

where $\dot{m}$ represents the evaporation rate of the solar evaporation generator, which is the net rate calculated by deducting the contribution of the dark state. Under 1 solar irradiation conditions, the evaporation rate of NiV_{15}@wood was 2.23 kg m^{-2} h^{-1}; h_{LV} is the total enthalpy change of the liquid-gas phase with sensible heat, which is 1446 J g^{-1} in this system as measured *via* differential scanning calorimetry (DSC); C_{opt} is the optical concentration of the solar simulator; and q_i is the nominal solar light intensity (1 kW m^{-2}). According to the above conditions, the evaporation efficiency of NiV_{15}@wood was calculated as ~90% under 1 solar irradiation.

RESULTS AND DISCUSSION

Morphological and structural characterization

Inspired by natural trees that absorb water from the ground

through transpiration, natural wood was chosen as a carrier for fabricating a solar water evaporation generator through the loading of polyoxovanadate with excellent surface photothermal properties (Fig. 1). The polyoxovanadate compound cluster NV_{15} with a mixed valence of vanadium was synthesized following a previously reported procedure [33], and its crystal structure was determined *via* single-crystal XRD [37]. NiV_{15} was obtained *via* an ion exchange reaction (the synthetic route and structure are shown in Fig. S1). We chose basswood with a rough surface (Fig. S2a) through the vertical transverse growth direction for water transport because its capillaries and tracheids (~10 μm) were arranged in the natural growth direction (Fig. S2b). Small pits of ~2 μm were distributed on the walls of the vessel channels and tracheid channels (Fig. S2c, d), which allowed for the lateral transport of substances. The photothermal material NiV_{15} was deposited on basswood *via* a two-step strategy. First, the wood chunk was soaked in NV_{15} aqueous solution and then dried so that NV_{15}@wood was obtained, with NV_{15} adsorbed on the surface of the wood pieces. Second, NV_{15}@wood was immersed into a $Ni(Phen)_3Cl_2$ aqueous solution at 80°C so that the adsorbed NV_{15} on the surface was fully converted into NiV_{15} *via* an ion exchange reaction. The insolubility of NiV_{15} in water prevented its loss during the evaporation process. The bilayer-structured NiV_{15}@wood composite comprised NiV_{15} attached to the outer surface of the wood, while the inner side of the wood channels remained almost blank, with scattered NiV_{15} particles (Fig. 2a–d). The top-view and cross-sectional SEM images of the elemental mapping confirmed the hollow bilayer structure, which allowed for the dual functions of solar-thermal conversion and water transport (Fig. 2e–l).

Optical properties of the solar evaporation generator

The solar absorbance capability is a decisive factor for efficient evaporation. The optical absorbances of raw wood and NiV_{15}@wood were measured *via* UV-vis-NIR spectroscopy (Fig. 3a).

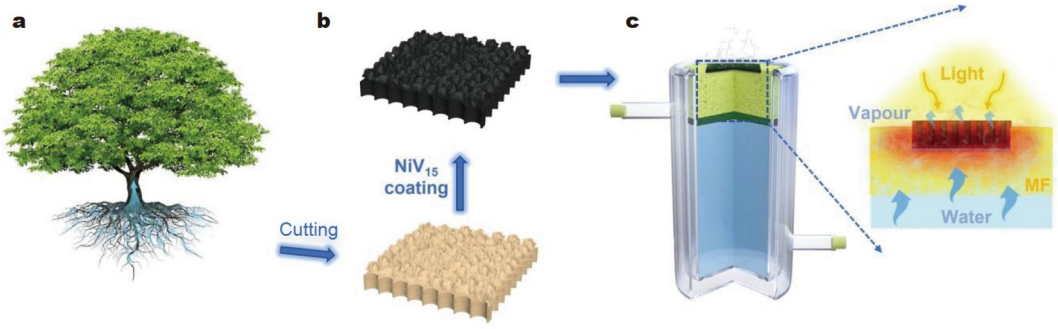

Figure 1 Schematic of heat management and water transportation. (a) Trees transport water upward from the bottom and absorb sunlight for photosynthesis. (b) The black surface of NiV_{15}@wood is obtained through the loading of NiV_{15} on the surface. (c) NiV_{15}@wood, insulation material, and a vacuum double-glass beaker were used to construct the NiV_{15}@wood-MF solar evaporation generator.

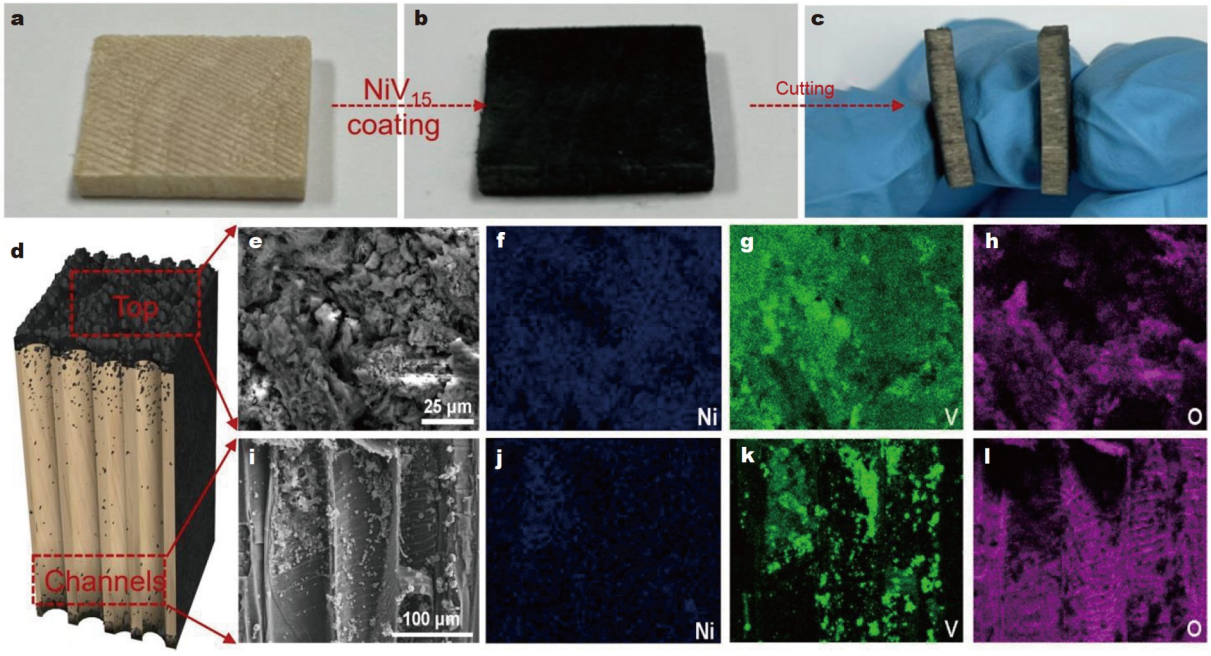

Figure 2 Photos of the raw wood (a) and NiV_{15}@wood (b). (c) NiV_{15}@wood was cut to reveal the body's natural wood color and the decorated wood's black surface. (d) Schematic of NiV_{15}@wood. (e) Top-view SEM images of NiV_{15}@wood and the mapping image of Ni, V, and O (f–h). (i) Cross-sectional SEM images of NiV_{15}@wood and its mapping image for Ni, V, and O (j–l).

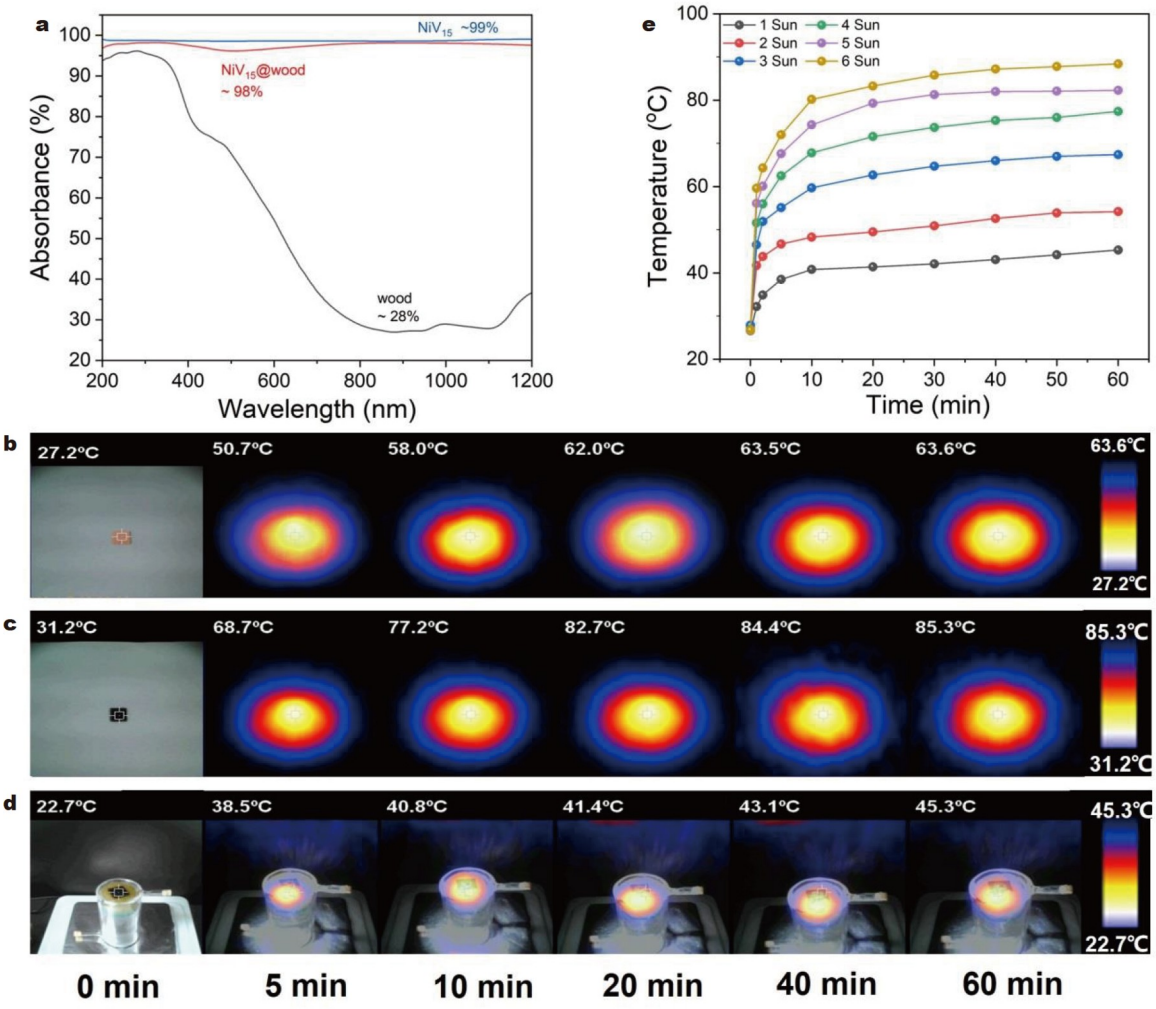

Figure 3 (a) UV-vis-NIR absorption spectra of the raw wood, NiV_{15}, and NiV_{15}@wood. Infrared thermography images of wood (b) and NiV_{15}@wood (c) under dry conditions and the evaporator (d) for different durations under 1 Sun. (e) The stable surface temperature of NiV_{15}@wood on the water under different solar concentrations of 1–6 Sun for 60 min (1 Sun = 1 C_{opt} = 1 kW m^{-2}).

Raw wood exhibited high absorbance in the UV region, and the absorbance declined in the visible range owing to the colored lignin in the plant cell walls [11], and light absorption was negligible in the NIR range. NiV_{15}@wood featured excellent absorbance in the full UV-vis-NIR spectrum because of the black NiV_{15}. The rough surface (Fig. S2a) absorbed, reflected, and scattered the photoirradiation, thereby achieving a high absorbance rate of >98%, which accounted for the fast and efficient solar evaporation performance. The actual surface temperatures of wood and NiV_{15}@wood under 1 Sun were monitored using an infrared thermometer (Fig. 3b, c). The surface temperature of wood reached ~50°C within 5 min and was stable at ~40 min (Fig. 3b). In sharp contrast, after 5 min of illumination, the surface temperature of NiV_{15}@wood rapidly increased to 68°C and remained at ~84°C after 20 min (Fig. 3c). The results showed that NiV_{15} played an important role in solar-thermal conversion, leading to a higher rate of temperature increase on the NiV_{15}@wood sample.

NiV_{15}@wood, with excellent photothermal conversion and fluent water transport passages, functioned as an efficient solar water evaporation chip. The chip was placed in a groove of MF with a suitable size to make it float on the upper layer of water. MF foam ensured sufficient water supply to wood owing to its macropores and prevented horizontal and vertical heat conduction owing to its insulation property. The solar evaporation generator concentrated the heat on the upper surface of the chip and reduced the heat transfer to the liquid below (Fig. 1c). During actual water evaporation using the solar evaporation generator, the irradiated surface exhibited a temperature of over 40°C on the surface after 10 min, consistent with the results monitored using an infrared thermometer (Fig. 3d). This is the highest temperature that the wood-based evaporator can reach under the same conditions. We also tested the surface temperature under irradiation with light intensities of 1–6 Sun. The NiV_{15}@wood solar evaporator was rapidly heated within 5 min (Fig. 3e). The maximum temperature was stabilized ~20 min after irradiation. With increasing light intensity from 1 to 6 Sun, the surface stabilization temperature increased from 45 to 88°C, with an approximately linear growth trend (Fig. S3).

Heat management in the solar evaporation generator

To achieve efficient water evaporation, optimizing heat management for efficient solar energy utilization is necessary. MF features high porosity, hydrophilicity, heat insulation, low cost,

and low density. In our experiments, MF foam with a diameter of 1.4 cm and a thickness of 2 cm was used. The temperature gradient under irradiation along the longitudinal direction was tested using the experimental setup shown in Fig. 4a–c. As shown in Fig. 4a, the top surface maintained the highest temperature, and the temperature at the upper part of 2 cm (MF part) was slightly lower than that at the top surface. The water temperature below the MF section decreases exponentially with the height of the evaporator. The temperature distribution under irradiation in the transverse direction is shown in Fig. 4b. The temperature of the entire NiV_{15}@wood area (0–0.7 cm) surface remains constant, while the surface temperature decreases slightly from the edge of NiV_{15}@wood to the edge of MF (0.7–1.5 cm). The sudden temperature drop (1.4–1.5 cm) confirms that MF could effectively reduce the heat exchange between NiV_{15}@wood and the MF peripheral aqueous solution. The direct observation of the temperature distribution over the whole device under the irradiation of 3 and 6 Sun was obtained by an infrared thermometer (Fig. 4c). The results indicate that the heat-insulating MF effectively maintained the photothermal energy on the evaporating surface in both the longitudinal and transverse directions and greatly reduced the heat transfer between NiV_{15}@wood and the surrounding water. Moreover, we used a double-layer vacuum beaker as a container to reduce the heat exchange between the evaporation system and the surrounding environment, leveraging the vacuum insulation property. Through the management of the NiV_{15}@wood-MF evaporation system, the heat energy obtained from the photothermal conversion was concentrated on the surface water layer, maximizing the use of energy for efficient and rapid evaporation.

Evaporation performance of the solar evaporation generator

According to the excellent photothermal conversion performance of NiV_{15} and the optimized heat management, water evaporation experiments were conducted using a xenon lamp as an artificial light source and an AM1.5 filter to simulate sunlight. The NiV_{15}@wood composite material was placed on the MF and combined with a glass device to construct the NiV_{15}@wood-MF solar evaporation generator (see details in S1.1 in the Supplementary information). A photo of the solar evaporation device is given in Fig. S4a. An electronic balance was used to monitor the mass change of the device in real time. The evaporation curves of NiV_{15}@wood-MF against irradiation time were recorded under various light intensities. All of the curves show that the liquid water mass decreased rapidly in the first 20 min, and the rate of vapor production gradually accelerated. After 20 min, the slope of the curve reached a maximum constant, and the evaporation rate was stable (Fig. 4d). With increasing light intensity from 1 to 6 Sun, the evaporation rate increased from 2.23 to 12.42 kg m^{-2} h^{-1} (see the EXPERIMENTAL SECTION for the calculation details and Fig. 4e for the calculation results). Water vapor steam generation was observed at 3 and 6 Sun, and the vapor production rates were accelerated with increasing light intensity (Fig. S4b, c, Videos S1 and S2). We also evaluated the vapor generation performance of pure water, MF, and wood-MF under the same conditions. They all exhibited much lower vapor generation rates than NiV_{15}@wood-MF, owing to the absence of the high-efficiency photothermal conversion material (Fig. 4e). In particular, all of the evaporation rates were the net evaporation contribution by subtracting the water evaporation in the dark (Fig. S5). The evaporation rate of NiV_{15}@wood-MF was 5.4

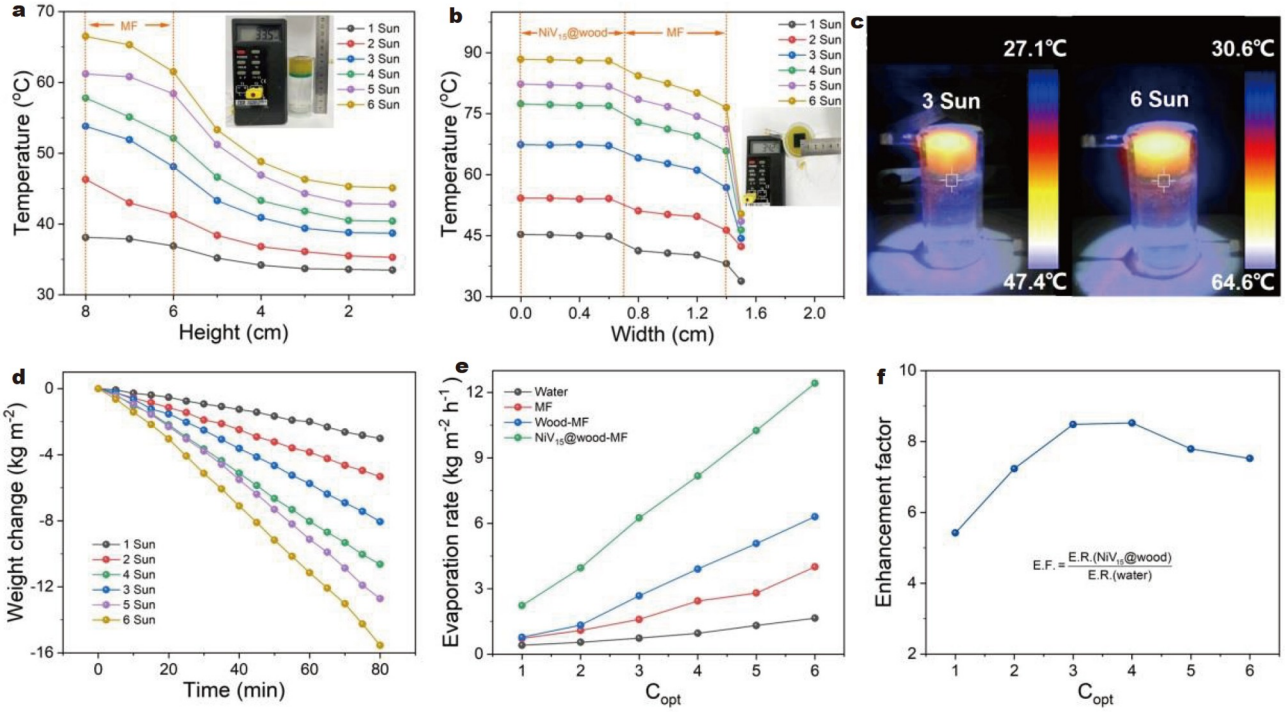

Figure 4 Water temperatures in the evaporator at various heights (a) and widths (b) under solar concentrations of 1–6 Sun. (c) Thermal infrared imaging of the longitudinal temperature distributions of the NiV_{15}@wood evaporation generator at 3 (left) and 6 (right) Sun. (d) Evaporation rates of pure water and different evaporators when exposed to the sun for different durations. (e) Evaporation rates of pure water and different evaporators when exposed to the sun for different durations. (f) Enhancement factor of NiV_{15}@wood compared with pure water.

and 8.5 times that of pure water under 1 and 4 Sun irradiation, respectively (Fig. 4f). The photothermal material NiV_{15} and the wooden chip carrier were introduced as essential factors to achieve efficient and rapid solar water evaporation. As calculated, the NiV_{15}@wood-MF solar evaporation generator achieved a thermal conversion efficiency (η) of 90% under 1 Sun and efficiently generated vapor under increased light intensities (see the EXPERIMENTAL SECTION for calculation details and Fig. 5a for the calculation results). The high-stability NiV_{15}@wood composite enabled continuous evaporation for a long period under working conditions. Moreover, we conducted a test of 10 cycles (eight hours for each cycle) under 1 Sun, and the results revealed no performance decay (Fig. 5b). A comparison of the PXRD results of NiV_{15}@wood before and after ten testing cycles (Fig. S6) reveals that the overall peak shape and position of NiV_{15}@wood did not change significantly and that NiV_{15}@wood maintained the same physical phase and remained stable after long-term water evaporation. This demonstrates the superior stability of NiV_{15}@wood in the solar evaporation process, which enables long-term and efficient water evaporation.

Evaporator practical application and desalination property

To test the desalination capacity of the NiV_{15}@wood-MF evaporation generator, water evaporation experiments were performed using artificial seawater (see details in S1.2). As shown in Fig. 5c, the concentrations of four ions (Na^+, Mg^{2+}, K^+, and Ca^{2+}) in the desalinated water were greatly reduced, fully meeting the drinking water standards specified by the World Health Organization [38]. In particular, the concentration of Na^+ ions was reduced by four orders of magnitude compared with the initial concentration (for details, see Table S1). The NiV_{15}@wood evaporation generator exhibited an excellent ability to resist salt precipitation. After 24-h continuous evaporation, no significant salt precipitation occurred on the NiV_{15}@wood-MF surface (Fig. S7), and the original pore structure was still retained, as revealed by SEM (Fig. S8), which allowed for long-term efficient water evaporation. We also conducted outdoor water evaporation experiments using natural sunlight instead of a Xe lamp light source (Fig. 5d and S1.3). The evaporation rates over pure water, MF, wood-MF, and NiV_{15}@wood-MF over continuous 5 h (Fig. 5e) were consistent with the laboratory test results. At a sunlight intensity of 0.6 kW m^{-2} (the outdoor temperature at 28°C), the stable water evaporation rate was ~1.7 kg m^{-2} h^{-1} over NiV_{15}@wood-MF, which was slightly higher than the results obtained under laboratory test conditions, owing to higher ambient temperatures. Compared with the other wood-based solar evaporation generators with diverse photothermal materials, including graphite, carbon nanotubes, and polypyrrole, the NiV_{15}@wood-MF evaporation system resulted in a much higher evaporation rate and higher evaporation efficiency (Fig. 5f, details in Table S2). Polymeric hydrogel [22] and nanostructured gel [23] evaporation systems have shown higher evaporation rates and higher evaporation efficiency. However, these systems were characterized by complicated fabrication procedures and high cost for practical applications.

Mechanism of the high-performance solar evaporation generator

The excellent performance of the NiV_{15}@wood-MF evaporation system was due to the advantages of the efficient photothermal material NiV_{15}, excellent heat management, and fluent water transport benefiting from the multiple channel structure of the wood. To reveal the mechanism of the excellent performance, we

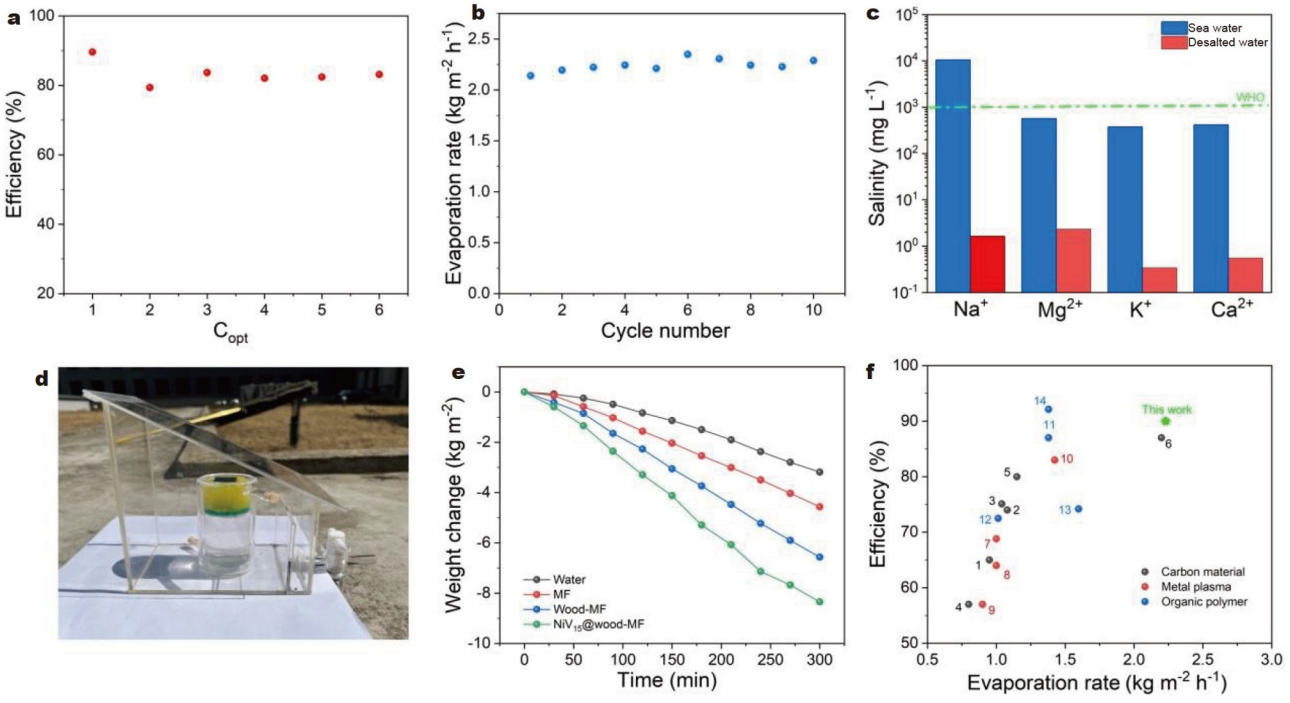

Figure 5 (a) Efficiency of solar steam generation using NiV_{15}@wood-MF at different solar concentrations. (b) Cyclic performance of NiV_{15}@wood under 1 Sun from artificial seawater (8 h for each cycle). (c) Ion concentrations of Na^+, Mg^{2+}, K^+, and Ca^{2+} in seawater and desalted water. (d) Digital photograph of a solar evaporation test conducted under sunlight. (e) Evaporation mass change of water in the NiV_{15}@wood steam generation device over time under natural sunlight. (f) Comparison of the solar evaporation performances of NiV_{15}@wood with those of previously reported materials under 1 Sun illumination.

explored the physicochemical properties of the system. First, the thermal conductivities of raw wood and NiV_{15}@wood were determined as 0.17 and 0.30 W m^{-1} K^{-1}, respectively, *via* the laser flash method (see details in S1.4 and Fig. S9). NiV_{15}@wood is comparable to those of previously reported carrier materials, such as wood films [8], carbon foam [39], porous graphene [40], metal-organic framework-derived carbon materials [41], and graphene oxide film [42] for solar evaporation generators. Such low thermal conductivity accounts for the highly efficient heat accumulation on the NiV_{15}@wood surface. Second, wood is highly hydrophilic, as it is mainly composed of cellulose, hemicellulose, and lignin with a large number of hydroxyl groups, which can absorb water more than two times its weight and thus ensure efficient water supply [21]. Furthermore, we tested the contact angle of water in the original wood and NiV_{15}@wood, and the results indicate that both had a high affinity to water (Fig. S10), which is fundamental for fast water transport to the surface for continuous and efficient evaporation. Finally, when molecules enter the macropores in the natural wood, water does not escape from the pore interior as individual water molecules but rather agglomerates into small clusters of several to tens of small molecules [26,43–46]. Consequently, the evaporation enthalpy of water confined in the hydrophilic channels of wood (1446 J g^{-1}) was significantly lower than that of pure water (2160 J g^{-1}), as measured *via* DSC (Fig. S11) and contributes to efficient solar steam generation. We also explored the effect of NiV_{15}@wood thickness on the performance of the solar evaporation generator. The wood thickness can affect water transport and heat management. According to the literature [21], a lower wood thickness increases the capillary-driven pressure gradient for rapid water replenishment; however, when the wood is too thin, the thermal binding capacity is reduced, resulting in more heat transfer to the solution below and heat loss. The experimental results revealed that at a NiV_{15}@wood thickness of <10 mm, the evaporation rate accelerated with decreasing thickness until the thickness approached the critical value (2 mm, Fig. S12). A further reduction in the thickness led to deteriorated evaporation performance. Therefore, we chose 2 mm as the optimal thickness to achieve efficient solar evaporation.

CONCLUSIONS

The NiV_{15}@wood-MF evaporation system exhibited the following advantages: (1) NiV_{15} exhibited superior photothermal conversion performance, with an absorption capacity of ~98% in the wavelength range of 200–1200 nm. (2) Wood was cut with a chainsaw to form a rough surface to increase the light-absorbing surface area and elongate the light path for multiple scattering absorption to enhance the light absorption capacity and improve the photothermal conversion performance. (3) The combination of the wood carrier, characterized by poor thermal conductivity, the vacuum double-layer glass beaker, and the horizontal and vertical insulation MF foam caused the whole solar evaporator heat to be concentrated on the wood surface as much as possible, reducing the energy losses associated with heat exchange with the environment, the wall, and the solution below. Owing to the above advantages, our wood-based solar evaporation system achieved rapid evaporation of 2.23 kg m^{-2} h^{-1} under 1 Sun and 90% efficient evaporation efficiency, which are among the highest values reported for wood-based solar evaporation systems. Thus, our wood-based system offers a green and efficient method for producing clean water to solve the problem of freshwater shortage.

Received 20 January 2023; accepted 20 March 2023; published online 30 May 2023

1 Mekonnen MM, Hoekstra AY. Blue water footprint linked to national consumption and international trade is unsustainable. Nat Food, 2020, 1: 792–800
2 Richter BD, Bartak D, Caldwell P, *et al.* Water scarcity and fish imperilment driven by beef production. Nat Sustain, 2020, 3: 319–328
3 Werber JR, Osuji CO, Elimelech M. Materials for next-generation desalination and water purification membranes. Nat Rev Mater, 2016, 1: 16018
4 Wang L, Boutilier MSH, Kidambi PR, *et al.* Fundamental transport mechanisms, fabrication and potential applications of nanoporous atomically thin membranes. Nat Nanotech, 2017, 12: 509–522
5 Cohen-Tanugi D, Grossman JC. Nanoporous graphene as a reverse osmosis membrane: Recent insights from theory and simulation. Desalination, 2015, 366: 59–70
6 Kalogirou S. Seawater desalination using renewable energy sources. Prog Energy Combust Sci, 2005, 31: 242–281
7 Tufa RA, Curcio E, Brauns E, *et al.* Membrane distillation and reverse electrodialysis for near-zero liquid discharge and low energy seawater desalination. J Membrane Sci, 2015, 496: 325–333
8 Chen C, Li Y, Song J, *et al.* Highly flexible and efficient solar steam generation device. Adv Mater, 2017, 29: 1701756
9 Lewis NS. Research opportunities to advance solar energy utilization. Science, 2016, 351: aad1920
10 Sun S, Tian Q, Mi HY, *et al.* Fabric-based all-weather-available photo-electro-thermal steam generator with high evaporation rate and salt resistance. Sci China Mater, 2022, 65: 2479–2490
11 Zhu M, Li Y, Chen F, *et al.* Plasmonic wood for high-efficiency solar steam generation. Adv Energy Mater, 2018, 8: 1701028
12 Chen M, Wu Y, Song W, *et al.* Plasmonic nanoparticle-embedded poly(*p*-phenylene benzobisoxazole) nanofibrous composite films for solar steam generation. Nanoscale, 2018, 10: 6186–6193
13 Zhou X, Guo Y, Zhao F, *et al.* Hydrogels as an emerging material platform for solar water purification. Acc Chem Res, 2019, 52: 3244–3253
14 Li T, Liu H, Zhao X, *et al.* Scalable and highly efficient mesoporous wood-based solar steam generation device: Localized heat, rapid water transport. Adv Funct Mater, 2018, 28: 1707134
15 Wang Z, Yan Y, Shen X, *et al.* A wood-polypyrrole composite as a photothermal conversion device for solar evaporation enhancement. J Mater Chem A, 2019, 7: 20706–20712
16 Wang X, Liu Q, Wu S, *et al.* Multilayer polypyrrole nanosheets with self-organized surface structures for flexible and efficient solar-thermal energy conversion. Adv Mater, 2019, 31: 1807716
17 Liu G, Xu J, Wang K. Solar water evaporation by black photothermal sheets. Nano Energy, 2017, 41: 269–284
18 Ni G, Zandavi SH, Javid SM, *et al.* A salt-rejecting floating solar still for low-cost desalination. Energy Environ Sci, 2018, 11: 1510–1519
19 Zhang H, Wang Y, Liu Y, *et al.* Efficient solar evaporation by $[Ni(phen)_3][V_{14}O_{34}Cl]Cl$ hybrid semiconductor confined in mesoporous glass. ChemSusChem, 2020, 13: 2945–2951
20 Guan QF, Han ZM, Ling ZC, *et al.* Sustainable wood-based hierarchical solar steam generator: A biomimetic design with reduced vaporization enthalpy of water. Nano Lett, 2020, 20: 5699–5704
21 Jia C, Li Y, Yang Z, *et al.* Rich mesostructures derived from natural woods for solar steam generation. Joule, 2017, 1: 588–599
22 Guo Y, Zhou X, Zhao F, *et al.* Synergistic energy nanoconfinement and water activation in hydrogels for efficient solar water desalination. ACS Nano, 2019, 13: 7913–7919
23 Zhao F, Zhou X, Shi Y, *et al.* Highly efficient solar vapour generation *via* hierarchically nanostructured gels. Nat Nanotech, 2018, 13: 489–495
24 Kuang Y, Chen C, He S, *et al.* A high-performance self-regenerating solar evaporator for continuous water desalination. Adv Mater, 2019, 31: 1900498

25 He S, Chen C, Kuang Y, *et al.* Nature-inspired salt resistant bimodal porous solar evaporator for efficient and stable water desalination. Energy Environ Sci, 2019, 12: 1558–1567
26 Zhang X, Yang L, Dang B, *et al.* Nature-inspired design: *p*-Toluenesulfonic acid-assisted hydrothermally engineered wood for solar steam generation. Nano Energy, 2020, 78: 105322
27 Zou H, Meng X, Zhao X, *et al.* Hofmeister effect-enhanced hydration chemistry of hydrogel for high-efficiency solar-driven interfacial desalination. Adv Mater, 2023, 35: 2207262
28 Lei C, Guan W, Guo Y, *et al.* Polyzwitterionic hydrogels for highly efficient high salinity solar desalination. Angew Chem Int Ed, 2022, 61: e202208487
29 Gao J, Cao S, Tay Q, *et al.* Molecule-based water-oxidation catalysts (WOCS): Cluster-size-dependent dye-sensitized polyoxometalates for visible-light-driven O_2 evolution. Sci Rep, 2013, 3: 1853
30 Wang Y, Liu C, Wang Y, *et al.* Efficient photo-thermo-electric conversion using polyoxovanadate in ionic liquid for low-grade heat utilization. ChemSusChem, 2021, 14: 5434–5441
31 Maiti D, Zhong J, Zhang Z, *et al.* Polyoxomolybdate (POM) nanoclusters with radiosensitizing and scintillating properties for low dose X-ray inducible radiation-radiodynamic therapy. Nanoscale Horiz, 2020, 5: 109–118
32 Ge G, Zheng Q, Li X. Multi-wall carbon nanotube-induced nanobelt potassium vanadate composite as cathode for sodium-ion batteries. Electrochim Acta, 2022, 430: 141128
33 Nunes GG, Bonatto AC, de Albuquerque CG, *et al.* Synthesis, characterization and chemoprotective activity of polyoxovanadates against DNA alkylation. J InOrg Biochem, 2012, 108: 36–46
34 Akrawi BA, Al-Allaf YO. Study of conductance of the ionic association phenomena of $[Ni(phen)_3]Cl_2$ in different solvents and different temperatures. Tik J Pure Sci, 2006, 11: 178–182
35 Wang Y, Zhang L, Wang P. Self-floating carbon nanotube membrane on macroporous silica substrate for highly efficient solar-driven interfacial water evaporation. ACS Sustain Chem Eng, 2016, 4: 1223–1230
36 Zhang P, Liao Q, Yao H, *et al.* Direct solar steam generation system for clean water production. Energy Storage Mater, 2019, 18: 429–446
37 The crystallographic information file (CIF) has been deposited in the cambridge crystallographic data centre with an ccdc# of 110187. https://www.ccdc.cam.ac.uk/structures/Search?Ccdcid=110187&DatabaseToSearch=Published
38 World Health Organization. (2011). Safe drinking-water from desalination. World Health Organization. https://apps.who.int/iris/bitstream/handle/10665/70621/WHO_HSE_WSH_11.03_eng.pdf?sequence=1&isAllowed=y
39 Ghasemi H, Ni G, Marconnet AM, *et al.* Solar steam generation by heat localization. Nat Commun, 2014, 5: 4449
40 Ito Y, Tanabe Y, Han J, *et al.* Multifunctional porous graphene for high-efficiency steam generation by heat localization. Adv Mater, 2015, 27: 4302–4307
41 He P, Hao L, Liu N, *et al.* Controllable synthesis of sea urchin-like carbon from metal-organic frameworks for advanced solar vapor generators. Chem Eng J, 2021, 423: 130268
42 Meng Y, Li H. Rational design of reduced graphene oxide film for solar thermal desalination. Water Supply, 2019, 19: 1704–1710
43 Miyazaki M, Fujii A, Ebata T, *et al.* Infrared spectroscopic evidence for protonated water clusters forming nanoscale cages. Science, 2004, 304: 1134–1137
44 Fujii A, Mizuse K. Infrared spectroscopic studies on hydrogen-bonded water networks in gas phase clusters. Int Rev Phys Chem, 2013, 32: 266–307
45 Liu Y, Yu S, Feng R, *et al.* A bioinspired, reusable, paper-based system for high-performance large-scale evaporation. Adv Mater, 2015, 27: 2768–2774
46 Liu N, Hao L, Zhang B, *et al.* Rational design of high-performance bilayer solar evaporator by using waste polyester-derived porous carbon-coated wood. Energy Environ Mater, 2022, 5: 617–626

Acknowledgements This work was supported by Hefei National Laboratory for Physical Sciences at the Microscale, Hefei Science Center of Chinese Academy of Sciences, Fujian Institute of Innovation of Chinese Academy of Sciences, the National Natural Science Foundation of China (NSFC, 21571167, 51502282 and 22075266), and the Fundamental Research Funds for the Central Universities (WK2060190053 and WK2060190100).

Author contributions Zhang T performed the experiments and wrote the manuscript with support from Liu B; Yan W and Liu C participated in the drawing design. Wang Y and Wang J proofread the manuscript. Ye F was responsible for the ion concentration detection. All authors contributed to the general discussion.

Conflict of interest The authors declare that they have no conflict of interest.

Supplementary information Experimental details and supporting data are available in the online version of the paper.

Tian Zhang is currently a Master's student at the University of Science and Technology of China. Her research interest focuses on the photothermal conversion mechanism of vanadium polyacids and their solar evaporation application.

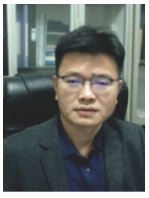

Bo Liu is a full professor at the University of Science and Technology of China. He was awarded a PhD degree from Kobe University in 2009. He completed the AvH postdoc research at Ruhr University and Karlsruher Institute of Technologie. In 2012, he moved to the University of Liverpool as a Marie Curie fellow. In 2015, Dr. Liu joined the University of Science and Technology of China. His research interests mainly focus on functional inorganic materials and energy conversion.

一种环境友好型高效木质钒多酸太阳能蒸发发生器

张恬, 严文, 王彦, 王洁, 刘聪妍, 叶飞, 刘波*

摘要 目前, 世界正面临着淡水匮乏的问题, 这是一个全球性的挑战, 而以低成本对海水进行净化、脱盐和蒸馏是解决这一挑战的关键. 由于天然木材具有高亲水性、低密度、微孔通道和低导热性等优点, 被广泛认为是太阳能蒸发的优良载体. 然而, 迄今为止报道的大多数木基太阳能蒸发器在低功率的太阳能照射下, 都呈现出经济效益不高, 蒸发效率有限的不足. 在此, 我们报道了一种生态友好并且高效蒸发的木基太阳能蒸发发生器, 它由优良光热转换性能的钒多酸附着在具有天然通道的木材表面复合而成. 该太阳能蒸发器在200–1200 nm的宽波长范围内均表现出优异的光吸收能力(~98%), 并且木材的绝热性最大限度地减少了散热. 同时木材天然通道能够提供快速的水传输, 降低了蒸发焓, 从而提高了整体蒸发效率. 在1个太阳光照下, 蒸汽产生速率为2.23 kg m^{-2} h^{-1}, 太阳能蒸发效率高达90%. 这种环保、低成本、高效率的蒸发发生器在太阳能脱盐和水净化的实际应用中具有巨大潜力.

